Real-Time Detection of Femtosecond Optical Pulse Sequences via Time-To-Space Conversion in the Lightwave Communications Band

Jung-Ho Chung, *Student Member, IEEE,* and Andrew M. Weiner, *Fellow, IEEE, Fellow, OSA*

***Abstract*—A spectral nonlinear optics time-to-space converter operating in the lightwave communications band is reported for the first time. We demonstrate serial-to-parallel conversion of short frames of femtosecond pulses, for the first time operating at a conversion efficiency level allowing direct electronic readout at a conversion rate of hundreds of megaframes/s in real time, without signal averaging and with good signal-to-noise ratio. The results demonstrate that applications such as real-time measurements of ultrafast optical data sequences and header recognition in ultrafast optical time-division-multiplexed (OTDM) packet networks are approaching feasibility. Moreover, we analyze tradeoffs between optical powers and data rates from a system perspective, which allows us to assess the challenges for scaling to parallel demultiplexing of bit-interleaved OTDM transmission systems.**

***Index Terms*—Optical signal processing, serial-to-parallel conversion, space–time processing, sum frequency generation, three-wave mixing, time-domain multiplexing/demultiplexing, time-to-space conversion, ultrafast optics, ultrafast pulse measurement.**

I. Introduction

OPTICAL time-division multiplexing (OTDM) is an essential technique for ultra-high-speed lightwave systems, together with wavelength-division multiplexing (WDM). The realization of ultrafast OTDM systems must be accompanied by the development of technologies in ultrashort optical pulse generation, high-speed modulation/detection, time-division multiplexing/demultiplexing, synchronization/clock recovery, and so on [1]. A number of impressive system experiments have been reported, including OTDM femtosecond pulse transmission at 640 Gb/s over 92 km of a dispersion-managed fiber [2]. All-optical time-division demultiplexers have been implemented using a variety of approaches, such as the optical Kerr effect in fiber, the nonlinear optical loop mirror, four-wave mixing (FWM) in a fiber or semiconductor laser amplifier (SLA), the Mach–Zehnder interferometer via SLAs, nonlinearities in multiple quantum well (MQW) semiconductor, cross-phase modulation, and an electroabsorption modulator, etc. [1]. Conventional OTDM demultiplexers aim at selecting a single channel out of multichannel OTDM data at a time. In some cases, however, it may be more efficient to perform simultaneous multichannel demultiplexing. In a few cases, this has been demonstrated using a tree structure (for example, [3]), which usually requires a complex integration, or by using TDM-to-WDM conversion (for example, [4]). However, space–time optical processing techniques [5]–[22], in which optical signals are processed simultaneously in the space domain and in the time and optical frequency domain, offer a simple but innovative approach with the potential to accomplish this multichannel demultiplexing. In this paper, we report an ultrafast time-to-space converter based on space–time processing, which is capable of serial-to-parallel conversion of an ultrafast optical data frame. Our time-to-space converter is the first to operate in the lightwave communications band.

In the last decade, space–time processing has received considerable attention in the ultrafast optics research community. Most of the research focuses on space-to-time or time-to-space conversion. Space-to-time (or parallel-to-serial) conversion generates an optical data stream using a spatial pattern [5]–[9]. This can be applied for the generation of data packets for slotted OTDM systems or for multiplexing of individual channels corresponding to spatial pattern elements (if the spatial elements are modulated at sufficient speeds) in bit-interleaved OTDM systems [23]. On the other hand, time-to-space (or serial-to-parallel) conversion can play a role mostly in the receiver side [10]–[22]. In time-to-space conversion, ultrafast optical temporal or serial waveforms are transformed into their spatial (parallel) equivalents. In slotted OTDM networks, time-to-space converters can potentially be used to perform header recognition. In bit-interleaved OTDM systems, time-to-space converters can potentially perform simultaneous multichannel demultiplexing. In addition to the capability for multichannel processing, the demultiplexer using time-to-space conversion may have better tolerance against timing jitter compared to some conventional demultiplexer techniques. In many conventional demultiplexers, sampling of an optical pulse off of its peak due to timing jitter leads to amplitude jitter, which degrades receiver performance. Some conventional demultiplexers minimize the effect of timing jitter by using group velocity walkoff between the data and sampling pulses [24]. However, the cost of this approach is that group velocity walkoff limits the interaction length between data and sampling pulses, which limits the ability to minimize switching energy. In time-to-space conversion, timing jitter causes transverse displacement of the optical signal on a

Manuscript received March 6, 2003; revised August 12, 2003. This research was supported in part by the U.S. Army Research Office under Contract DAAD19-00-0497, in part by the National Science Foundation under Contract 0100949-ECS, in part by Intel Corporation, and in part by the sponsors of the Center for Education and Research in Information Assurance and Security.

The authors are with the School of Electrical and Computer Engineering, Purdue University, West Lafayette, IN 47907-2035 USA (jchung@ecn.purdue.edu).

Digital Object Identifier 10.1109/JLT.2003.820042

detection plane. As long as the jitter remains much less than the bit period, each detector at the detection plane can have an active area larger than the maximum displacement induced by timing jitter, which minimizes the power penalty. An important point is that this immunity to timing jitter comes automatically, without the need to trade off against switching energy.

Note that this time-to-space conversion technique requires a synchronized short reference pulse. In situations where that is not already available, the reference pulse can be generated via optical clock recovery techniques [1], or it may be possible to transmit the reference along with the signal data over the same fiber [14], [17]. Further, in the case of ultrashort pulse transmission over fibers, dispersion is important. Fortunately, methods to compensate dispersion for pulses as short as a few hundred femtoseconds have been demonstrated for distances at least into tens of kilometers [25], [26]. In addition, dispersion effects can also be compensated in part within the converter [14].

Time-to-space conversion also has gained interest as a new approach for ultrafast optical waveform measurement, since it can display pulse waveforms in the space domain. Picosecond optical pulses constituting several hundred gigabit/second OTDM data have been measured usually using optical sampling techniques [27]–[29], where the signal to be measured is mixed with optical sampling pulses having a very short pulse width, low timing jitter, and repetition frequency slightly detuned from that of the signal to be measured. One limitation of the sampling techniques is that the output corresponds to an average over many waveforms and repetitive signals are required. In contrast, time-to-space conversion can be used even for measuring single, nonrepetitive waveforms, since each signal pulse is mapped one-to-one into its spatial replica with no averaging effect. In the femtosecond regime, one popular waveform measurement technique is frequency-resolved optical gating (FROG) [30], where a pulse is sampled by a gate function derived from the pulse itself in order to generate a two-dimensional time-frequency trace. FROG is capable of determining essentially unique waveform information including phase. However, this technique requires an iterative computer routine to extract waveform data from the time-frequency trace. Spectral phase interferometry for direct electric-field reconstruction (SPIDER) is another well-known femtosecond pulse characterization technique. SPIDER does not require iterative algorithms, and a single-shot kilohertz SPIDER was recently demonstrated [31]. However, some computer processing is still required, which will likely preclude operation at the gigaframe/second rates of interest for optical communications, and the ability to characterize signals as complex as multibit sequences is yet to be demonstrated. In contrast, in time-to-space conversion, complete intensity data are obtained in parallel directly on a single-shot basis without any software processing; only the power budget limits the processing rate.

Various methods have been proposed to implement time-to-space converters [10]–[22]. Most of them are based on spectral holography or spectral nonlinear optics [10]–[21]. In the early 1990s, picosecond-regime time-to-space mapping was demonstrated by Ema and his coworkers via FWM in a thin ZnSe film [10]. Their recent experiment was performed with femtosecond pulses at faster conversion rates [19]. The first mapping of femtosecond pulses was demonstrated in a spectral holography setup using a MQW photorefractive device by Nuss *et al.* [11]. This spectral holography based approach was subsequently pursued in Fainman's group [12], [17], who also demonstrated time-to-space conversion based on spectral nonlinear optics via three-wave mixing (TWM) [13], [14], [18], [20], [21] and FWM [21] in nonlinear crystals. The demonstration of a TWM converter [13] was an important advance, because the fast response of the electronic nonlinearity involved in the $\chi^{(2)}$ process in principle permits operation with independent data frames arriving at high repetition rates (e.g., Gframes/s). In an experiment using TWM in a potassium niobate ($KNbO_3$) crystal, our group has achieved the highest conversion efficiency that has ever been reported in spectral nonlinear optics using low-energy high-repetition-rate sources [15], [16], which is key for operation at realistic power budgets in high-speed systems. This publication also presented the key principles for optimizing the nonlinear sensitivity in the unusual geometry of a spectral nonlinear time-to-space converter [15]. We note that direct gating of femtosecond pulses using the optical Kerr effect in nonlinear materials in a single-shot cross-correlation geometry is also being studied as a time-to-space conversion scheme [22].

In spite of the diverse research activity on time-to-space converters, as reviewed above, significant challenges must be overcome before they can find application in real-world lightwave communication networks. First of all, current optical communication networks require time-to-space conversion to operate with 1.5-μm input pulses, whereas all previous experiments were performed with visible or near-infrared light sources below $\sim$ 1 μm. Moreover, practical converter systems should have an intrinsically fast nonlinear conversion process and a sensitivity that can scale to $\sim$Gframes/s conversion rate at realistic pulse energies (i.e., $\sim$nJ per frame or less). The latter requirement has not been addressed in most previous works. For example, in experiments demonstrating the principles of various interesting spectral nonlinear optics space–time processors, a femtosecond pulse amplifier with submillijoule pulse energies at a 1-KHz rate was used [20], [21]. In this paper, we report the first spectral nonlinear optical time-to-space converter operating at optical communications wavelengths. We demonstrate that its conversion efficiency is large enough for direct real-time measurement of short frames of $\sim$0.5-Tb/s ultrafast optical data on a single-shot basis with good signal-to-noise ratio (SNR) at a conversion rate of 0.5-Gframes/s. Moreover, we show that the measured characteristics of our converter are in good agreement with the theory. Finally, we analyze the scaling of the time-to-space converter for various frame rates, peak bit rates, etc., with an emphasis on the optical power requirements. Our analysis indicates that the power requirement is the key issue in scaling to higher data and frame rates and identifies an interesting tradeoff between optical power and the degree of parallelism.

The rest of this paper is structured as follows. In Section II, we will discuss and analyze theoretically the principle of the time-to-space conversion. In Section III, we will describe the experimental setup, present our results, and compare with the

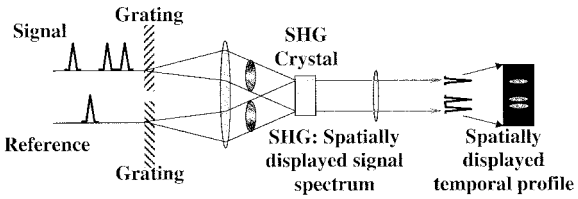

Fig. 1. The schematic of the time-to-space converter.

theory. This section discusses basic time-to-space operation, conversion efficiency, and demonstration of real-time detection of the output signal at high conversion rates. In Section IV, we estimate the power requirements of a fully operating system, making use of the results on nonlinear optical conversion efficiency discussed in the earlier sections of this paper. Conclusions are given in Section V.

II. Principle and Theoretical Analysis

A. Principle

This time-to-space converter employs the 4-f pulse shaper arrangement as shown conceptually in Fig. 1, which is similar to those in [13]–[16], [20], and [21]. Shaped or unshaped signal pulses and unshaped reference pulses are incident onto respective gratings oriented symmetrically with respect to the optical axis. Thus, the rays that diffract in the high-diffraction-efficiency $+1$ order can be utilized in both beams in order to generate spectral dispersions that are opposite in sign for signal and reference beams. Each wavelength component in each spectrally dispersed beam is focused through the first lens and separated from one another at the back Fourier plane, where the nonlinear crystal for second harmonic generation (SHG) is located. At any given transverse location in the crystal, the pulse is stretched in time by a factor corresponding to the ratio of the spatial extent of the spectrum to the beam radius of an individual wavelength component—i.e., the pulse duration at the spectral dispersion plane is inversely proportional to spectral resolution of the setup [5], [8]. The crystal generates a nonlinear polarization proportional to the product of the two electric fields corresponding to the overlapping signal and reference wavelength components. This nonlinear polarization in turn induces the second harmonic (SH) field. The center frequency components at frequency ω_0 in each of the beams are aligned to intersect at the Fourier plane. Frequency components in the signal beam that are offset from the center frequency by a specific amount overlap spatially with frequency components of the reference beam that are offset by an equal but opposite amount. Then via sum frequency mixing (SFM) in the crystal, a quasi-monochromatic SH beam with a narrow spectrum around $2\omega_0$ is generated. The SH field induced by the nonlinear polarization propagates along the optical axis because the transverse components of the wave vectors from the signal and reference beams cancel out. The second lens performs the spatial Fourier transform of the SH field emerging from the crystal, with the spatial Fourier transform resulting at the back focal plane of the lens.

If we assume that the reference pulse is sufficiently short, its power spectrum will be very wide compared to the signal spectrum. Then the nonlinear polarization generated in the crystal in the transverse direction corresponds to a scaled version of the signal spectrum—i.e., a spatially displayed temporal Fourier transform of the signal pulse. The spatial profile of the SH field at the output of the crystal is also equal to a scaled version of the complex spectrum of the signal pulse. Therefore, the spatial Fourier transform due to the second lens corresponds to the inverse Fourier transform of the spectrum—i.e., the original temporal waveform of the signal pulse. Thus, the SH field at the back focal plane represents a spatially displayed version of the signal pulse temporal waveform. If the width of the reference pulse is comparable to that of the signal pulse, the output image will spatially display the electric-field cross-correlation between signal and reference pulses rather than the signal pulse directly.

B. Theoretical Analysis

This experiment is theoretically analyzed following the approach in the previous literature from our group [16]. A related analysis by Fainman's group was published in [13]. For convenience's sake, important formulas are rewritten here with minor modifications as necessary. The electric fields of input signal and reference beams as functions of time t and a spatial coordinate $\tilde{x}$ transverse to the beam propagation direction are, respectively, expressed as

$$e_s(\tilde{x},t) = Re\left[a_s(t)e^{\frac{-\tilde{x}^2}{w_{in}^2}}e^{j\omega_0 t}\right] \tag{1}$$

and

$$e_r(\tilde{x},t) = Re\left[a_r(t)e^{\frac{-\tilde{x}^2}{w_{in}^2}}e^{j\omega_0 t}\right]. \tag{2}$$

Here $a_s(t)$ and $a_r(t)$ are slowly varying complex envelope functions, w_{in} is the beam radius under the assumption of a Gaussian spatial profile, and ω_0 is the center angular frequency. The signal and reference electric fields at the back focal plane of the first lens with a focal length of f_1 as functions of time t and a spatial coordinate x (perpendicular to the optical axis) are, respectively, given by

$$e'_s(x,t) \sim Re\left[e^{j\omega_0 t}\int d\omega e^{j\omega t}A_s(\omega)e^{\frac{-(x-\alpha\omega)^2}{w_0^2}}\right] \tag{3}$$

and

$$e'_r(x,t) \sim Re\left[e^{j\omega_0 t}\int d\omega e^{j\omega t}A_r(\omega)e^{\frac{-(x+\alpha\omega)^2}{w_0^2}}\right] \tag{4}$$

where $A_s(\omega)$ is the temporal Fourier transform of $a_s(t)$, $A_r(\omega)$ is that of $a_r(t)$, and α and w_0 are the spatial dispersion parameter and the focused spot size, respectively, given by

$$\alpha = \frac{\lambda^2 f_1}{2\pi c d\cos\theta_d} \tag{5}$$

and

$$w_0 = \frac{\cos\theta_{in} f_1 \lambda}{\cos\theta_d \pi w_{in}}. \tag{6}$$

Here c is the speed of light, d is the grating period, and θ_{in} and θ_d are incident and diffracted angles at each grating [16]. In

(1)–(4), phase terms representing the noncollinear geometry are neglected because these terms cancel out when multiplied together to form the nonlinear polarization. The SH field emerging from the crystal is given by

$$e'_{\mathrm{SHG}}(x,t) \sim Re\left[e^{j2\omega_0 t}\int d\Omega e^{j\Omega t} e^{-\frac{1}{2}\left(\frac{\alpha\Omega}{w_0}\right)^2} H_{\mathrm{PM}}(\Omega) \times \int d\omega_1 A_s(\omega_1) A_r(\Omega-\omega_1) e^{\frac{-2\left[x+\frac{\alpha}{2}(\Omega-2\omega_1)^2\right]}{w_0^2}}\right] \tag{7}$$

where Ω is the sum-frequency offset from $2\omega_0$ and $H_{\mathrm{PM}}(\Omega)$ represents the filtering function due to the finite phase-matching bandwidth of the nonlinear crystal. Finally, in the back focal plane of the second lens, the spatial Fourier transform of the field in (7) is obtained, which is expressed as

$$e''_{\mathrm{SHG}}(x,t) \sim Re\left[e^{j2\omega_0 t} B(x) C(x,t) D(x)\right] \tag{8}$$

where

$$B(x) = e^{-\frac{1}{8}(\beta w_0 x)^2} \tag{9}$$

$$C(x,t) = \int d\Omega e^{j\Omega\left(t+\frac{\alpha\beta x}{2}\right)} H_{\mathrm{PM}}(\Omega) e^{-\frac{1}{2}\left(\frac{\alpha\Omega}{w_0}\right)^2} \tag{10}$$

and

$$D(x) = \int dx' a_s(\alpha\beta x') a_r\left(\alpha\beta(x'+x)\right). \tag{11}$$

Here, $\beta = 2\omega_0/cf_2$ is the Fourier transform scale factor introduced by the second lens with a focal length of f_2. $D(x)$ represents the time-to-space mapping function of the output SH field, whereas $B(x)$ and $C(x,t)$ represent the finite spatial aperture and the temporal profile of the output field, respectively. In (11), $D(x)$ is given by the cross-correlation between $a_s(t)$ and $a_r(t)$, with t replaced by $\alpha\beta x$. This yields the time-to-space mapping factor, i.e.,

$$(\alpha\beta)^{-1} = \frac{f_2}{f_1}\frac{cd\cos\theta_d}{2\lambda}. \tag{12}$$

The spatial profile function $B(x)$ in (9) implies that the intensity of the time-to-space output image falls off for the transverse locations farther from center. This creates a finite spatial window, whose intensity full-width at half-maximum (FWHM) is given by

$$\Delta X = \frac{4\sqrt{\ln 2}}{\beta w_0} = \frac{\sqrt{\ln 2} f_2 w_{in}\cos\theta_d}{f_1\cos\theta_{in}}. \tag{13}$$

Likewise, there exists a temporal window for the original signal beam, which corresponds to the temporal counterpart of the spatial window in the above. Dividing ΔX in (13) by $(\alpha\beta)^{-1}$ in (12), we obtain the FWHM of the temporal window, i.e.,

$$\Delta T = \frac{4\alpha\sqrt{\ln 2}}{w_0} = \frac{2\sqrt{\ln 2} w_{in}\lambda}{cd\cos\theta_{in}}. \tag{14}$$

This window is much larger than the original pulse duration, resulting from the stretching of the pulse due to the spectral dispersion. A sequence of multiple signal pulses can be converted with a single reference pulse as long as the total time duration of the signal pulse sequence falls within this temporal window. The center of this time aperture coincides with the time location of the reference pulse. This time window effect is closely related to the finite time window that is well known in femtosecond pulse shaping [5], [8], which is related to the spatial resolution of the pulse-shaping apparatus.

Usually the time-to-space output image will be detected by a time-integrating detector. However, sometimes we may be interested in its time dependence, which is represented by $C(x,t)$ in (10). This expression contains the phase-matching spectral response function $H_{\mathrm{PM}}(\Omega)$, which can be expressed by

$$H_{\mathrm{PM}}(\Omega) = \frac{\sin\left(\frac{\Delta k L_{\mathrm{eff}}}{2}\right)}{\frac{\Delta k L_{\mathrm{eff}}}{2}} \tag{15}$$

where the phase mismatch Δk is given by $\Delta k = \delta\nu\Omega$ with $\delta\nu$ the group velocity mismatch and L_{eff} the effective nonlinear interaction length [16]. Plugging (15) into (10) and noting that (10) results in the temporal convolution between the inverse Fourier transform of $H_{\mathrm{PM}}(\Omega)$ and that of $\exp[-(1/2)(\alpha\Omega/w_0)^2]$, we obtain

$$C(x,t) \propto \int dt' \mathrm{rect}\left(\frac{2t'}{\delta\nu L_{\mathrm{eff}}}\right) \times \exp\left[-\frac{w_0^2}{2\alpha^2}\left(t+\frac{\alpha\beta x}{2}-t'\right)^2\right] \tag{16}$$

where $\mathrm{rect}(t/\tau) = 1$ if $|t| \le \tau$ and $\mathrm{rect}(t/\tau) = 0$ otherwise. Thus, $C(x,t)$ expresses explicitly the temporal waveform of the output SH field.

III. Experimental Setup and Results

A. Experimental Setup

The schematic of the detailed experimental setup is shown in Fig. 2. As mentioned above, this time-to-space converter uses a communications-band laser source. A beam of femtosecond pulses with an FWHM of $t_p = \sim 200$ fs and a pulse energy of $\sim$2.5 nJ at a repetition rate of 80 MHz and a center wavelength of $\lambda = 1560$ nm is emitted out of an optical parametric oscillator (OPO) (Opal, Spectra Physics Inc.). The beam is first spatially expanded to have an input beam radius of $w_{in} = 3.0$ mm. According to (13) and (14), the larger the input beam radius is, the wider the temporal or spatial window is. The beam is then split into two arms: one for the signal and the other for the reference. The signal pulse may be shaped or unshaped. Fig. 2(a) illustrates the whole setup in the unshaped case. For the shaped case, in this paper, we simply introduced the so-called optical multiplexer [32], consisting of three beam splitters and four delay lines to generate four serial pulses. This simple pulse shaper is shown in Fig. 2(b). The reference pulse, on the contrary, only passes through a delay line in order to adjust its temporal delay with respect to the signal pulse(s). Then, each beam is incident with an angle of $\theta_{in} = 42.0^\circ$ on the respective reflection grating with a groove frequency of $d^{-1} = 830$ mm^{-1} and a diffraction efficiency of $\sim$90%. Here the center-to-center beam separation at the grating surfaces along the x-axis is $\sim$9 mm. The center wavelength component of the beam that diffracts in $+1$ order

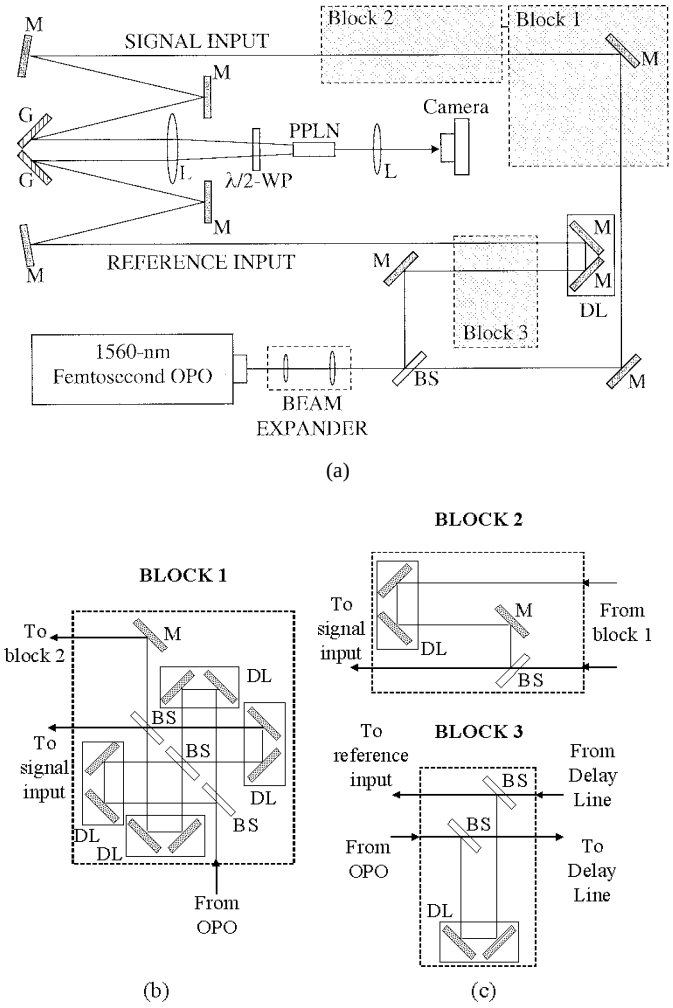

Fig. 2. Detailed experimental setups for (a) the case of unshaped signal pulses, (b) an optical multiplexor replacing Block 1 in (a) in the case of shaped signal pulses, and (c) the replacements for Block 2 and 3 in (a) for second frame and reference generation (M: mirror, G: grating, L: lens, WP: waveplate, PPLN: periodically poled lithium niobate, BS: beam splitter, DL: delay line, OPO: optical parametric oscillator).

emerges from the grating with an angle of $\theta_d = 38.7°$. The gratings are aligned so that the center components from both beams propagate in parallel until passing the first lens. The lens with a focal length of $f_1 = 254$ mm causes both spectrally dispersed beams to focus at the Fourier plane, where they intersect at a full angle of $\rho = 2.14°$.

A periodically poled lithium niobate (PPLN) crystal was used for the SHG crystal located at the Fourier plane. It has a width of 5 mm, a height of 0.5 mm, and a length of $L = 20$ mm, and its quasi-phase-matching (QPM) grating period is $\Lambda = 19$ μm at room temperature. Usually a PPLN crystal has a nonlinear coefficient of $d_{33} = 27$ pm/V, a refractive index of $n = \sim 2.15$ for all three waves polarized along the z-axis, and a group velocity mismatch of $\delta\nu = 0.30$ ps/mm at 1.56 μm [33]. The PPLN crystal is contained inside a temperature-controlled aluminum oven for phase matching. PPLN crystals are usually designed so that all interacting beams are extraordinary rays. Since a horizontal polarization was required for efficient diffraction from the gratings, a half-wave plate is placed in front of

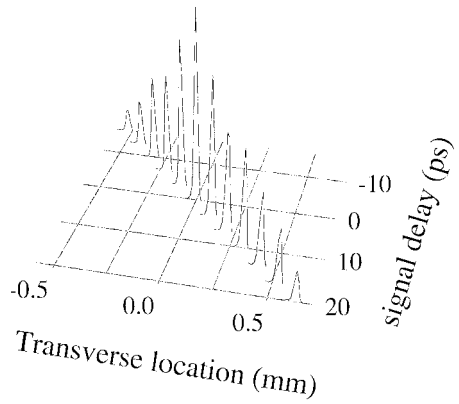

Fig. 3. The relative power of the output red signal as a function of the transverse location and the delay of the signal pulse with respect to the reference pulse. The mapping factor is 31.3 μm/ps and the FWHM temporal window is 24.9 ps.

the crystal to convert to the vertical polarization needed at the PPLN. The waveplate imposes a maximum reflectance loss of 0.25% per surface. The quasi-monochromatic SH field coming out of the crystal oscillates at an optical frequency of $2\omega_0$ or a wavelength of 780 nm. The second lens with a focal length of $f_2 = 90.2$ mm spatially Fourier-transforms the red SH light, producing the spatial replica of the signal field at its Fourier plane. The parameters described up to now give spatial dispersion parameter $\alpha = 3.49 \cdot 10^{-14}$ cm/Hz from (5), focused beam radius $w_0 = 40.0$ μm from (6), and Fourier transform scale factor $\beta = 2\omega_0/cf_2 = 8.93 \cdot 10^3$ cm^{-2}.

B. Experimental Results

In this section, we present time-to-space converter images and other data showing that the operation of our time-to-space is in line with theoretical expectations. These data confirm that our apparatus, which is the first to operate in the lightwave band, works in accord with previous experiments operating in the visible or near visible [13]–[16], [18], [20], [21]. We then emphasize studies of the nonlinear sensitivity and the ability to operate at hundreds of megaframes/second, which is a unique contribution of our work.

1) Time-To-Space Mapping Factor and Time Window: The time-to-space mapping factor was investigated using unshaped, identical signal and reference pulses as shown in Fig. 2(a). While adjusting the temporal delay of the reference pulse with respect to the signal pulse, the output power and transverse location of the red SH field at the image plane are measured with a camera made up of a silicon detector array assisted with an analysis tool (beam profiler, Photon, Inc.). The output power plotted as a function of position is shown in Fig. 3 for various relative delays. A linear relationship between the SH spatial location and the temporal delay is observed, with a slope corresponding to a time-to-space mapping factor of 31.3 μm/ps. Also, by observing the rolloff in output intensity for large delays, we can estimate an FWHM temporal window of $\Delta T = 24.9$ ps. From (12) and (14) with the parameters given in the previous section, the mapping factor and FWHM temporal window are estimated at $(\alpha\beta)^{-1} = 32.1$ μm/ps and $\Delta T = 29.1$ ps, respectively. Thus, the data are in reasonably

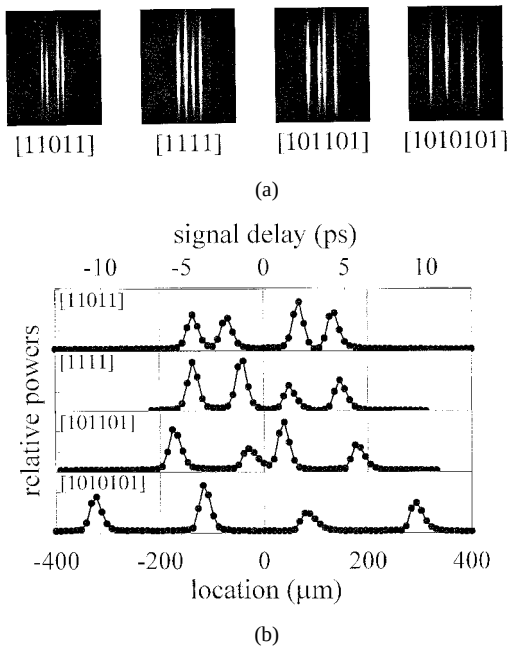

Fig. 4. The (a) images and (b) horizontally cut intensity profiles of multibit conversion output, corresponding to bit sequences of {11 011}, {1111}, {101 101}, and {1 010 101}.

good agreement with the theoretical estimates. We note that the camera pixel width is 9.77 μm. This limits the time resolution to $\sim$312 fs. This limit can be avoided using a larger focal length for the second lens f_2 to spread the image more widely over the detector array.

2) Time-To-Space Output Images: To observe output images of multibit data frames, the signal pulse is shaped using an optical multiplexor. This corresponds to the experimental setup in Fig. 2(a), with Block 1 replaced by the optical multiplexor shown in Fig. 2(b), where the output beam path to Block 2 is neglected in this case. The camera mentioned above is still used for taking the image data. A different combination of delays in the multiplexer gives a different combination of bits in a frame. This multiplexor producing four pulses with adjustable delays is sufficient for the purpose of the current experiment. In future experiments, programmable femtosecond pulse shapers, such as the Fourier transform pulse shaper [34] or the direct space-to-time pulse shaper [7]–[9], can potentially be employed to generate more complex data packets. Fig. 4 shows examples of resulting output images for bit sequences {11 011}, {1111}, {101 101}, and {1 010 101}, formed around the center of the temporal window. In Fig. 4(a), the images are vertical lines because the vertical dimension is not subject to the conversion process, as explained in the previous section. For this reason, the vertical dimension may be used for further signal processing [22]. Each intensity profile shown in Fig. 4(b) is obtained by a horizontal line cut through the corresponding image in Fig. 4(a). This corresponds to the cross-correlation between the signal waveform and the reference pulse, as expected in (11). The nonuniformity of the pulse heights is caused by slightly different beam paths of the multiplexed pulses owing to small misalignments of the optical multiplexer. The graphs have two horizontal axes, one for time and the other for space, aligned

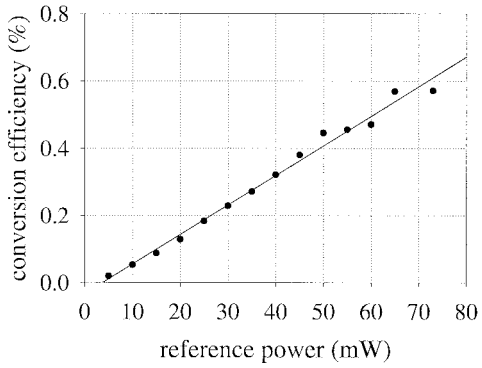

Fig. 5. The conversion efficiency as a function of the reference power. The slope corresponds to $\sim$8.8%/W or $\sim$0.7%/nJ.

using the measured mapping factor 31.3 μm/ps—i.e., 68.9-μm peak spacing in the first profile implies 2.2-ps temporal interval between input pulses. These profiles shows that each bit can be distinguished without aliasing at bit separations shorter than $\sim$2 ps, which corresponds to a peak data speed of $\sim$0.5 Tb/s. Better temporal resolution down to the input pulse width should be easily obtained, simply by expanding the output beam on the detector or charge-coupled-device array.

3) Conversion Efficiency: Conversion efficiency was obtained by dividing the power of the input signal beam, measured after the wave plate, by the SH power, measured after the second lens in the configuration shown in Fig. 2(a). The loss caused by the grating and waveplate is $\sim$10%, so this does not have a strong effect on the overall conversion efficiency. Fig. 5 shows the dependence of the conversion efficiency on the average reference power, with the signal power fixed at $\sim$71 mW and the temperature for the PPLN crystal fixed at $\sim$ 107 °C. The slope shows a linear relationship with a slope of $\sim$ 8.8%/W ($\sim$0.7%/nJ). At our maximum reference power of 73 mW, the conversion efficiency is $\sim$0.6%. Although the overall efficiency is less than obtained in our previous work [15], we will demonstrate later that this efficiency is already large enough for electronic readout on a single-shot basis.

According to the formulation established in our prior work [15], the efficiency η for a single signal pulse near the center of the temporal window in the collinear geometry scales with the experimental parameters in the following way:

$$\eta = \sin^2 \sqrt{\frac{\kappa d_{\text{eff}}^2 U_r t_p L_{\text{eff}}^2}{n^2 \lambda^3 \Delta T^2 b}} \tag{17}$$

where $\kappa = 90.5\pi^2/c\varepsilon_0$ is a proportionality constant, d_{eff} is the effective nonlinear coefficient, U_r is the reference pulse energy, $b = 2\pi n w_0^2/\lambda$ is the confocal length, L_{eff} is the effective nonlinear interaction length, and ΔT is the FWHM temporal window size. This formula is valid for a collinear geometry under the assumption that the group velocity walkoff between fundamental and SH waves is small compared to ΔT, which is inversely proportional to the spectral resolution of the optical setup. This condition is at least approximately true in our experiments. The experiment of [15] was performed in a collinear geometry and with approximately optimum focusing, for which we set $L_{\text{eff}} \approx b$. Using the parameters listed in the first row in

TABLE I
COMPARISON OF EXPERIMENTAL PARAMETERS AND RESULTING CONVERSION EFFICIENCIES BETWEEN OUR PREVIOUS [15] AND CURRENT EXPERIMENTS. $KNbO_3$ AND PPLN STAND FOR POTASSIUM NIOBATE AND PERIODICALLY POLED LITHIUM NIOBATE, RESPECTIVELY, WHICH ARE THE NONLINEAR MATERIALS USED IN THE TWO EXPERIMENTS. WE TAKE $d_{\text{eff}} = (2/\pi)d_{33}$ FOR PPLN WITH FIRST-ORDER QPM. NOTE THAT THE PREVIOUS EXPERIMENT WAS PERFORMED IN A COLLINEAR GEOMETRY, FOR WHICH THE EFFECTIVE INTERACTION LENGTH L_{eff} IS SET EQUAL TO b [15], WHILE THE CURRENT EXPERIMENT IS PERFORMED IN A NONLINEAR GEOMETRY. TO ACCOUNT FOR THIS, WE SET $L_{\text{eff}} \approx b/\sqrt{2}$

Reference	λ (μm)	d_{eff} (pm/V)	t_p (fs)	b (mm)	L_{eff} (mm)	n	ΔT (ps)	U_r (nJ)	η (%)	
									Calc'd	Meas'd
[15]	0.86	20 ($KNbO_3$)	125	2.8	b	2.28	3.9	2	96	58
Current work	1.56	17.2 (PPLN)	200	13.8	$b/\sqrt{2}$	2.15	25	0.9	1.1	0.6

Table I, (17) predicts an efficiency of 96% at $U_r = 2$ nJ, the maximum energy available in that experiment. This compares favorably with the measured value of 58%. Our current experiment uses a noncollinear geometry, with an attempt made to minimize the angle between beams. As pointed out in [20], in a noncollinear geometry with distinguishable signal and reference beams, there may be an extra factor of two in the efficiency equation. The analysis of [20] is limited to a thin nonlinear crystal. However, in our experiments, the noncollinear beams begin to spatially separate within the thick nonlinear crystal, which we account for approximately by setting $L_{\text{eff}} \approx b/\sqrt{2}$. The level of approximation in (17) is consistent with the approximation involved in our treatment of the noncollinear interaction. Now applying (17) with the experimental parameters listed in the second row of Table I, we calculate an efficiency of 1.1% at our maximum reference energy of $U_r = 0.9$ nJ. Once again this is in reasonable agreement with the experimental efficiency ($\sim$0.6%). These results show that (17) remains reasonably accurate over a variation in the experimental parameters, giving rise to a two order of magnitude variation in conversion efficiency. Consequently, we can use (17) to estimate the power requirements for time-to-space conversion in a full system context, which we discuss in Section IV.

An interesting point is that (17) shows a relationship between efficiency, pulse width, and time window [15]. In particular, efficiency goes down as the time window is increased. This relationship was developed further in [20].

4) Real-Time Detection of the Converted Signal at High Conversion Rates: Importantly, our efficiency is already sufficient for real-time observation of the output SH signal on a single-shot basis at high conversion rates without signal averaging. First, in the setup in Fig. 2(a), with Block 1 given by Fig. 2(b), we demonstrate an averaging-free single-shot measurement at a conversion rate equal to the laser repetition rate (80 MHz). One of the four spatially displaced pulses in the time-to-space output image is chosen to be detected using an avalanche photodiode (APD, C5658 Hamamatsu). With 800-nm input light, the APD has a quantum efficiency of 70%, a sensitivity of $2.5 \cdot 10^5$ V/W, including the avalanche and transimpedance amplifier gain, and a bandwidth of 1 GHz. Since an individual signal pulse has an average power of $\sim$9 mW (112.5-pJ energy per signal pulse), leading to an SHG output power of ~ 50 μW at $U_r = 0.9$ nJ, both signal and reference beams are attenuated to prevent the damage of the APD, whose maximum allowable continuous-wave input power is 10 μW. Fig. 6(a) shows the output of the APD recorded by a 500-MHz digital oscilloscope. Individual pulses at the 80-MHz repetition rate of the source laser are clearly visible with high SNR with no signal averaging. The $\sim$700-ps pulse shape results from the limited bandwidth of the oscilloscope and APD.

The possibility of operation at high frame rates approaching 1 Gframe/s was demonstrated using the experimental configuration in Fig. 2(a) with Blocks 1, 2, and 3 given by the setups in Fig. 2(b) and (c). Block 2 in Fig. 2(c) introduces a second data frame using the formerly unused output from the optical multiplexor. The separation of the second data frame from the first frame is set to be $\sim$2 ns. Likewise, Block 3 in Fig. 2(c) is for generating a second reference pulse, with its separation also set to $\sim$2 ns. In this case, the average power and the energy of any one individual pulse are $\sim$4 mW and $\sim$50 pJ for the signal beam and $\sim$18 mW and $\sim$220 pJ for the reference beam, respectively. Mixing of an individual signal waveform and reference pulse generates a time-to-space converter SHG output with an average power of ~ 5 μW. If the temporal separation between the first and second data frames is exactly matched to that of the two reference pulses, then at the converter output plane, the spatial images generated by successive data frames separated by $\sim$2 ns are perfectly aligned. On the contrary, if we introduce a slight positive or negative delay offset to the second data frame by adjusting the delay line shown in Fig. 2(c), then the successive images obtained with 2-ns separation will be slightly translated along the x-axis.

Fig. 6(b) and (c) shows oscilloscope traces of the APD output, with the APD set at a specific position in the image plane. Fig. 6(b) corresponds to the case when the reference pulse and signal frame separations are exactly matched. The inset, consisting of two slices extracted from the image of bit sequence {1 010 101}, illustrates that the APD, indicated by the arrow, detects bit 1's from both data frames. On the contrary, Fig. 6(c) results from the case when the second data frame has a small time offset, causing the two resulting images to be misaligned. The inset illustrates that the APD detects bit 1 in the

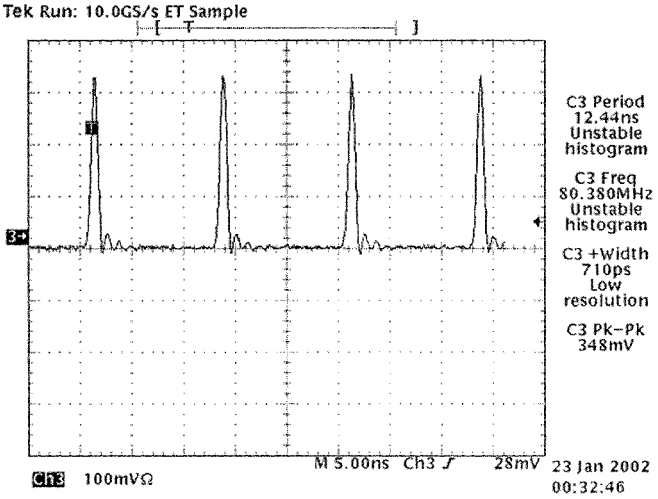

(a)

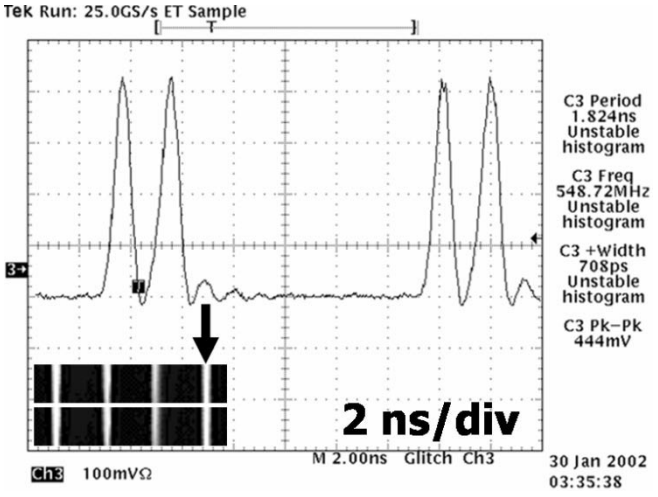

(b)

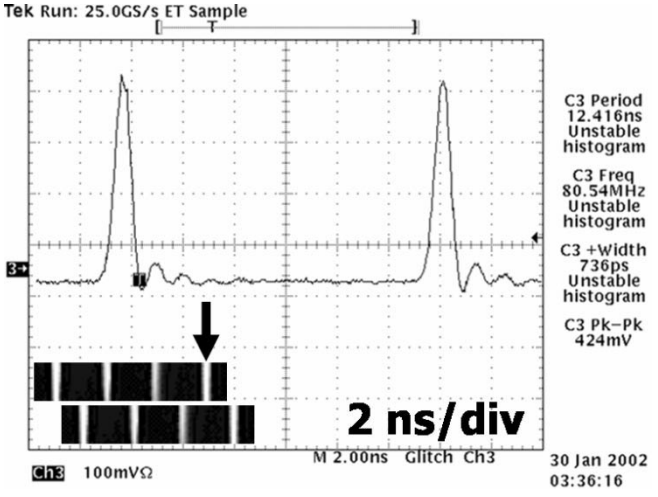

(c)

Fig. 6. Digital oscilloscope traces when the APD measures (a) a single channel of the output image resulting from the mixing of a data frame and a reference pulse at 80-MHz repetition rate, (b) bit 1's in both frames, and (c) bit 1 in the first frame and bit 0 in the second frame in the case when two data frames and two reference pulses with ~2 ns separations interact at 80-MHz repetition rate. Pairs of data frames separated by <2 ns are resolved, which corresponds to 0.5 Gframes/s. The insets from pairs of conversion images of the bit sequence {1 010 101} illustrate different time offsets between the reference pulses and data frames. The arrow represents the spatial location sampled by the APD.

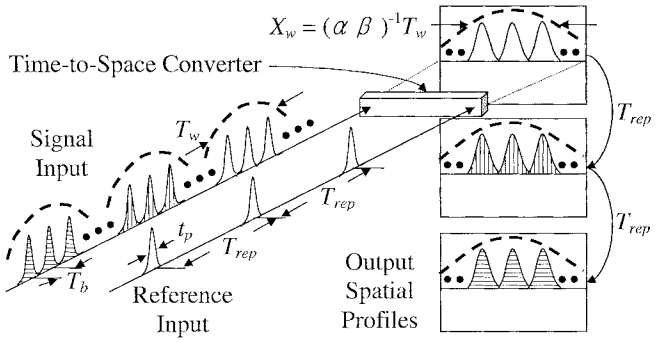

Fig. 7. The schematic showing the relationship between time constants, such as pulse duration, bit separation, repetition rate, and temporal window.

first frame and bit 0 in the second frame. From Fig. 6(b) and (c), pairs of data frames separated by < 2 ns are resolved, which corresponds to a peak conversion rate of 0.5 Gframes/s. This response is limited by the bandwidth of the APD and oscilloscope. A faster frame-to-frame response can be obtained by using electronics with higher time resolution. The frame rate is ultimately constrained by the system power budget, which is discussed in Section IV. We note that the duration of the temporal output waveform from (16) $C(x,t)$ turns out to be also of order ΔT. Thus, its finite duration does not add any additional constraint to the conversion rate from the system-level point of view because frames are not repeated any faster than ΔT, as will be discussed in Section IV.

The important result from these experiments is that sufficient nonlinear optical conversion efficiency can be obtained to permit single-shot real-time detection with no signal averaging for pulse energies in the subnanojoule range at hundreds of megaframes/second. Although a previous spectral nonlinear optics experiment also demonstrated high conversion efficiency with the potential for real-time detection exploiting the fast electronic nonlinearity of the $\chi^{(2)}$ process, that demonstration utilized submillijoule pulse energies at 1-KHz rate [20].

IV. System-Level Discussion

Fig. 7 illustrates a general time-to-space converter system operating on data frames that occur every $T_{\rm rep}$ s. Data frames consist of bits made up of Gaussian pulses (pulsewidth t_p), spread by bit separation T_b, and occupying a total temporal window T_w. Here T_w is chosen to give an integer number of bits per frame, namely, $N_b = T_w/T_b$, but need not be equal to the FWHM temporal aperture ΔT determined by the spectral resolution of the time-to-space converter. At the output image plane, the data contained in the time window T_w are mapped into their spatial equivalent having a spatial window of $X_w = (\alpha\beta)^{-1}T_w$. Of course, some pulses outside the boundaries of a single data frame of width T_w may also be converted. However, active detectors will be installed only for the output confined in the spatial window X_w; therefore, pulses outside the boundaries of a particular data frame are not detected. We can envision two principal system applications for the time-to-space converter. The first is for reading or processing of headers in an OTDM packet network. The distinguishing characteristic of the header processing system is that the width T_w of the frame operated on

by the time-to-space converter is much less than the repetition period $T_{\rm rep}$ of such frames (since generally the payload in the packet will be larger than the header). The second application is for demultiplexing of bit-interleaved OTDM data. Here the number of bits N_b in the frame is taken to be equal to the number of OTDM channels. Furthermore, the data frames arrive continuously, so that $T_{\rm rep} = T_w$. In this case, the detector array should be carefully aligned so that after the N_bth detector receives the last bit of a data frame, namely, a bit in channel N_b, the first detector receives the right next bit now contained in the subsequent data frame, namely, a bit in channel 1. In the following, we will estimate the power requirements for such system applications of time-to-space converters.

Now we assume that the output time-to-space image is detected by an array of N_b time-integrating detectors, each of which receives the full SH energy corresponding to a signal pulse. The relation $X_w = (\alpha\beta)^{-1}T_w$ allows each detector to be as wide as X_w/N_b, in which case the tolerance against timing jitter is maximized. We note, however, that the use of large-area detectors must be balanced against any degradation of the electronic response. In the presence of large jitter, the number of bits per frame N_b may be decreased to prevent crosstalk, which in turn decreases the conversion rate. Now let us assume that the pulse image peaks are located at $x_k = -X_w/2 + (X_w/N_b)(k - 1/2)$, $k = 1, 2, \ldots, N_b$. In the low conversion limit, (17) can be rewritten as

$$\eta = \frac{U_{\rm SHG}}{U_s} = \frac{\kappa' d_{\rm eff}^2 U_r t_p L_{\rm eff}^2}{n^2\lambda^3 \Delta T^2 b} \tag{18}$$

where κ' is the same as κ, but reduced to include the effect of any fixed insertion loss in the optical components. This expression gives the efficiency for the signal pulse located at the center of the temporal (or spatial) window. When we take into account the Gaussian window in (9), the SHG energy for the kth pulse is given by

$$U_{{\rm SHG},k} = e^{-\frac{1}{4}(\beta w_0 x_k)^2}\eta U_s = e^{-4\ln 2\left(\frac{t_k}{\Delta T}\right)^2}\eta U_s \tag{19}$$

where t_k is the time at the kth pulse peak, satisfying the relation $t_k = (\alpha\beta)x_k$. This equation implies that for fixed experimental parameters, the output SH energy per pulse decreases as x goes from zero (center of the window) to $\pm X_w/2$ (edges of the spatial window). We see that in choosing the spatial window size X_w, there is a tradeoff between the number of bits per frame (which we desire to be as large as possible for a fixed reference energy) and the magnitude of the variation in detected energies across the frame. This relationship was also explained in [20].

One constraint in the time-to-space conversion system is that the SHG energy of the outmost pulse in the spatial window should exceed the receiver sensitivity, expressed in terms of the minimum detectable optical energy, given by $U_{\rm min}$. That is

$$U_{{\rm SHG},1} = U_{{\rm SHG},N_b} \approx e^{-\ln 2\left(\frac{T_w}{\Delta T}\right)^2}\eta U_s \geq U_{\rm min} \tag{20}$$

where we take $t_1 \approx -T_w/2$ and $t_{N_b} \approx T_w/2$ (valid assuming $N_b \gg 1$). The average signal and reference powers can be written as $\overline{P}_s = (1/2)(N_b U_s/T_{\rm rep})$ and $\overline{P}_r = U_r/T_{\rm rep}$, respectively, where a factor of 1/2 is introduced into the signal power by assuming that the half of the signal bits are "0." Then combining (18) and (20), we obtain after some simplification

$$\overline{P}_s \cdot \overline{P}_r \geq \frac{n^2\lambda^3}{2\kappa' d_{\rm eff}^2}\frac{b}{L_{\rm eff}^2}\frac{N_b T_w^2 U_{\rm min}}{T_{\rm rep}^2 t_p}\left(\frac{\Delta T}{T_w}\right)^2 e^{\ln 2\left(\frac{T_w}{\Delta T}\right)^2}. \tag{21}$$

Let us now select the temporal window size T_w in order to minimize the system power requirements. Since $f(x) = x^{-2}e^{(\ln 2)x^2}$ has its minimum at $x = 1/\sqrt{\ln 2} \approx 1.2$, the required power is minimized when the frame duration T_w is approximately 1.2 times larger than the FWHM temporal window ΔT of the time-to-space converter response. Returning to (20), the rolloff at the edges of the window becomes simply e^{-1}. Equation (21) is rewritten as

$$\overline{P}_s \cdot \overline{P}_r \geq \frac{0.94 n^2\lambda^3}{\kappa' d_{\rm eff}^2}\frac{b}{L_{\rm eff}^2}\frac{N_b T_w^2 U_{\rm min}}{T_{\rm rep}^2 t_p}. \tag{22}$$

Equation (22) can be used to estimate time-to-space converter requirements over a wide range of nonlinear optical and system conditions.

As one example, we can use the parameters in the current experimental setup, as listed in the second row of Table I. Here we set $\kappa' = 0.8\,\kappa$ and take $L_{\rm eff} = b/\sqrt{2}$ to account for the noncollinear geometry. This results in

$$\overline{P}_s \cdot \overline{P}_r \geq \frac{(30.0\ {\rm W}) N_b T_w^2 U_{\rm min}}{T_{rep}^2 t_p} \tag{23}$$

where $T_w = 1.2\Delta T$.

Now let us consider the case of a header recognition system, where $T_w \ll T_{\rm rep}$. In this case we may vary N_b, t_p, T_w, and $T_{\rm rep}$ independently in (23). In Fig. 8, we plot the required average reference power as a function of the average signal power for $T_w = 31.25$ ps, $T_{\rm rep} = 3.125$ ns, and $U_{\rm min} = 5$ fJ, which corresponds to a reasonably good telecommunications receiver. Different values of the remaining parameters N_b and t_p are considered, such as $(N_b, t_p) = (10, 1{\rm ps})$, (10, 600 fs), (20, 500 fs), and (20, 300 fs). These curves imply, for example, that for a 31.25-ps-long header consisting of 10 bits with a pulse width of 1 ps in 320-GHz OTDM transmission, a reference power of 15 mW is required at a signal power of 10 mW. For a header

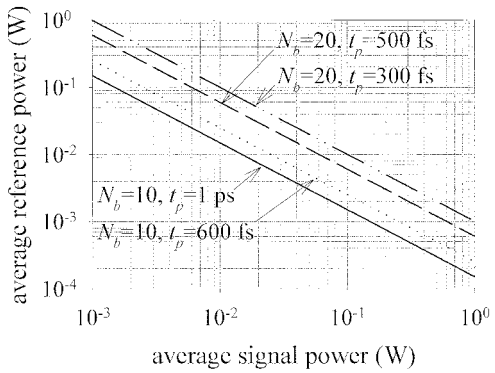

Fig. 8. Simulated curves of the minimum average reference power as a function of the minimum average signal power in the cases of header recognition in OTDM networks, where $T_w \ll T_{\rm rep}$ is assumed. The solid, dotted, dashed, and dash-dot lines correspond to the cases when $(N_b, t_p) = (10, 1{\rm ps})$, (10, 600 fs), (20, 500 fs), and (20, 300 fs), respectively.

containing 20 bits with 300-fs pulses in 640-GHz OTDM transmission, $\overline{P}_r \geq 100$ mW at the same signal power.

We note here that only the part of the signal power in the header is considered for this estimate, regardless of the power of the payload. The power would be reduced for lower rate systems, e.g., 100 Gb/s. These powers, although high, may already be implementable for some special purpose applications. However, it would be desirable to reduce the power requirements. Possibilities include using a more sensitive detector as well as a longer nonlinear crystal (PPLN crystals up to 5.5-cm length have been demonstrated [35]). More fundamentally, it would be advantageous to fabricate planar waveguides in PPLN or other SHG media. Provided such light could be coupled into such waveguides with low loss, we anticipate that the required $\overline{P}_s \cdot \overline{P}_r$ product could be reduced by approximately two orders of magnitude. We note that it may be advantageous to increase $\overline{P}_r$ and decrease $\overline{P}_s$ proportionally, since it will likely be easier to obtain high power in a local oscillator (the reference) located in the receiver where it does not have to be transmitted through fiber. In this case the reduction of the signal power would help to minimize nonlinearities in fiber-based transmission. Finally, power requirements are further reduced for longer input pulses and lower bit rates, e.g., 2-ps pulses and 100 Gb/s.

The most challenging situation is when $T_w = T_{\mathrm{rep}}$, which corresponds to demultiplexing a series of continuous frames with one frame coming right after the other. In this case, (23) leads to $\overline{P}_s \cdot \overline{P}_r \geq (30.0\,\mathrm{W}) N_b U_{\min}/t_p$. Under the assumption of $U_{\min} = 5$ fJ as above, $\overline{P}_r \geq 500$ mW at $\overline{P}_s = 500$ mW if $N_b = 5$ and $t_p = 3$ ps (simultaneous five-channel demultiplexing in 160-GHz OTDM transmission) and $\overline{P}_r \geq 3$ W at $\overline{P}_s = 500$ mW if $N_b = 10$ and $t_p = 1$ ps (simultaneous ten-channel demultiplexing in 320-GHz OTDM transmission). These powers are clearly higher than desirable, which points to the need to further optimize conversion efficiency, e.g., using planar waveguides as mentioned above.

Finally, we note that in (21)–(23), the power scales as $\sqrt{N_b}$ and is minimized by setting $N_b = 1$, which corresponds to bit-by-bit conversion. These equations, which we built on (17), are valid as long as the temporal window ΔT is larger than the group velocity walkoff in the SHG crystal. In PPLN at 1560-nm input, the walkoff is 0.3 ps/mm, as mentioned in Section III, giving a total walkoff of 6 ps (18 ps) in a 2-cm (6-cm) crystal. Therefore, we anticipate that ΔT should exceed the walkoff in most cases of interest. We see then that though time-to-space conversion does allow parallel processing, it does not reduce optical power requirements. There is a tradeoff between the degree of parallelism, which allows one to operate at rates faster than the individual receiver modules, and the required optical power. Nevertheless, the scaling of the optical power with degree of parallelism (N_b) is fundamentally more favorable than with other parallel methods, such as single-shot cross-correlation schemes.

V. Conclusion

Processing of optical data in the space domain as well as in the time domain may help overcome many obstacles that pure time-domain processing has confronted. Particularly, time-to-space conversion has the potential for simultaneous multichannel demultiplexing in OTDM networks. In addition, the demultiplexer based on this technique may be less sensitive to timing jitter than some conventional techniques. Time-to-space conversion can also play a role as a fast pulse waveform measurement technique, where the single-shot measurement is enabled. For those applications, the time-to-space converter should operate in the optical communications band with the capability for high-speed conversion at realistic power.

In this paper, we report a time-to-space converter based on spectral nonlinear optics, which operates for the first time in 1.5-μm optical communications bands. The operation of our time-to-space converter is in good agreement with theoretical predictions. We demonstrated time-to-space conversion of short frames of femtosecond pulses with $\sim$500-Gbs/s data speed at a conversion rate of hundreds of megaframes/s. Our time-to-space converter operated with the conversion efficiency large enough for direct electronic readout of the output signal at high conversion rates in real time, without signal averaging and with good SNR.

In addition, we analyzed the scaling of the time-to-space converters for various system parameters, which highlights the importance of the power requirement in time-to-space operation with high data and frame rates. The analysis, which shows tradeoffs between optical power and the degree of parallelism from a system perspective, indicates that the nonlinear conversion efficiency is already close to the regime needed for certain real-world lightwave applications, such as real-time optical pulse waveform measurements and header recognition in ultrafast OTDM networks. The analysis also allows one to estimate the power improvement required for full-channel demultiplexing of bit-interleaved OTDM transmission systems.

References

[1] S. Kawanishi, "Ultrahigh-speed optical time-division-multiplexed transmission technology based on optical signal processing," *IEEE J. Quantum Electron.*, vol. 34, pp. 2064–2079, Nov. 1998.

[2] T. Yamamoto, E. Yoshida, K. R. Tamura, K. Yonenaga, and M. Nakazawa, "640-Gbit/s optical TDM transmission over 92 km through a dispersion-managed fiber consisting of single-mode fiber and reverse dispersion fiber," *IEEE. Photon. Technol. Lett.*, vol. 12, pp. 353–355, Mar. 2000.

[3] C. Schubert, J. Berger, U. Feiste, R. Ludwig, C. Schmidt, and H. G. Weber, "160-Gb/s polarization insensitive all-optical demultiplexing using a gain-transparent ultrafast nonlinear interferometer (GT-UNI)," *IEEE Photon. Technol. Lett.*, vol. 13, pp. 1200–1202, Nov. 2001.

[4] K. Uchiyama, H. Takara, K. Mori, and T. Morioka, "160 Gbit/s all-optical time-division demultiplexing utilising modified multiple-output OTDM demultiplexer (MOXIC)," *Electron. Lett.*, vol. 38, pp. 1190–1191, Sep. 2002.

[5] A. M. Weiner, "High-resolution femtosecond pulse shaping," *J. Opt. Soc. Amer. B*, vol. 5, pp. 1563–1572, Aug. 1988.

[6] Y. Ding, D. D. Nolte, M. R. Melloch, and A. M. Weiner, "Time-domain image processing using dynamic holography," *IEEE J. Select. Topics Quantum Electron.*, vol. 4, pp. 332–341, Mar./Apr. 1998.

[7] D. M. Marom, D. Panasenko, P.-C. Sun, and Y. Fainman, "Spatial-temporal wave mixing for space-time conversion," *Opt. Lett.*, vol. 24, pp. 563–565, Apr. 1999.

[8] A. M. Weiner, "Femtosecond pulse shaping using spatial light modulators," *Rev. Sci. Instrum.*, vol. 71, pp. 1929–1960, May 2000.

[9] D. E. Leaird and A. M. Weiner, "Femtosecond direct space-to-time pulse shaping," *IEEE J. Quantum Electron.*, vol. 37, pp. 494–504, Apr. 2001.

[10] K. Ema, M. Kuwata-Gonokami, and F. Shimizu, "All-optical sub-Tbits/s serial-to-parallel conversion using excitons giant nonlinearity," *Appl. Phys. Lett.*, vol. 59, pp. 2799–2801, Nov. 1991.
[11] M. C. Nuss, M. Li, T. H. Chiu, A. M. Weiner, and A. Partovi, "Time-to-space mapping of femtosecond pulses," *Opt. Lett.*, vol. 19, pp. 664–666, May 1994.
[12] P. C. Sun, Y. T. Mazurenko, W. S. C. Chang, P. K. L. Yu, and Y. Fainman, "All-optical parallel-to-serial conversion by holographic spatial-to-temporal frequency encoding," *Opt. Lett.*, vol. 20, pp. 1728–1730, Aug. 1995.
[13] P. C. Sun, Y. T. Mazurenko, and Y. Fainman, "Femtosecond pulse imaging: ultrafast optical oscilloscope," *J. Opt. Soc. Amer. A*, vol. 14, pp. 1159–1170, May 1997.
[14] ——, "Real-time one-dimensional coherent imaging through single-mode fibers by space-time conversion processors," *Opt. Lett.*, vol. 22, pp. 1861–1863, Dec. 1997.
[15] A. M. Kan'an and A. M. Weiner, "Efficient time-to-space conversion of femtosecond optical pulses," *J. Opt. Soc. Amer. B*, vol. 5, pp. 1242–1245, Mar. 1998.
[16] A. M. Weiner and A. M. Kan'an, "Femtosecond pulse shaping for synthesis, processing, and time-to-space conversion of ultrafast optical waveforms," *IEEE J. Select. Topics Quantum Electron.*, vol. 4, pp. 317–331, Mar./Apr. 1998.
[17] D. M. Marom, P. C. Sun, and Y. Fainman, "Analysis of spatial-temporal converters for all-optical communication links," *Appl. Opt.*, vol. 37, pp. 2858–2868, May 1998.
[18] K. Oba, P. C. Sun, Y. T. Mazurenko, and Y. Fainman, "Femtosecond single-shot correlation system: a time-domain approach," *Appl. Opt.*, vol. 38, pp. 3810–3817, Jun. 1999.
[19] J. Ishi, H. Kunugita, K. Ema, T. Ban, and T. Kondo, "Time-to-space conversion of Tbits/s optical pulses using a self-organized quantum-well material," *Appl. Phys. Lett.*, vol. 77, pp. 3487–3489, Nov. 2000.
[20] D. M. Marom, D. Panasenko, P. C. Sun, and Y. Fainman, "Linear and nonlinear operation of a time-to-space processor," *J. Opt. Soc. Amer. A*, vol. 18, pp. 448–458, Feb. 2001.
[21] D. M. Marom, D. Panasenko, P. C. Sun, Y. T. Mazurenko, and Y. Fainman, "Real-time spatial-temporal signal processing with optical nonlinearities," *IEEE J. Select. Topics Quantum Electron.*, vol. 7, pp. 683–693, July/Aug. 2001.
[22] Y. Sato, M. Furuki, M. Tian, I. Iwasa, and L. S. Pu, "Improvement of on/off ratio in single-shot multichannel demultiplexing by using an optical Kerr gate of a squarylium dye J aggregate film," *Appl. Phys. Lett.*, vol. 80, pp. 2254–2256, Apr. 2002.
[23] V. W. S. Chan, K. L. Hall, E. Modiano, and K. A. Rauschenbach, "Architectures and technologies for high-speed optical data networks," *J. Lightwave Technol.*, vol. 16, pp. 2146–2168, Dec. 1998.
[24] K. Uchiyama, T. Morioka, S. Kawanishi, H. Takara, and M. Saruwatari, "Signal-to-noise ratio analysis of 100 Gb/s demultiplexing using nonlinear optical loop mirror," *J. Lightwave Technol.*, vol. 15, pp. 194–201, Feb. 1997.
[25] S. Shen and A. M. Weiner, "Complete dispersion compensation for 400-fs pulse transmission over 10-km fiber link using dispersion compensating fiber and spectral phase equalizer," *IEEE Photon. Technol. Lett.*, vol. 11, pp. 827–829, July 1999.
[26] E. Yoshida, T. Yamamoto, A. Sahara, and M. Nakazawa, "320 Gbit/s TDM transmission over 120 km using 400 fs pulse train," *Electron. Lett.*, vol. 34, pp. 1004–1005, May 1998.
[27] H. Ohta, N. Banjo, N. Yamada, S. Nogiwa, and Y. Yanagisawa, "Measuring eye diagram of 320 Gbit/s optical signal by optical sampling using passively modelocked fiber laser," *Electron. Lett.*, vol. 37, pp. 1541–1542, Dec. 2001.
[28] S. Kawanishi, T. Yamamoto, M. Nakazawa, and M. M. Fejer, "High sensitivity waveform measurement with optical sampling using quasiphase-matched mixing in $LiNbO_3$ waveguide," *Electron. Lett.*, vol. 37, pp. 842–844, June 2001.
[29] K. L. Deng, R. J. Runser, I. Glesk, and P. R. Prucnal, "Single-shot optical sampling oscilloscope for ultrafast optical waveforms," *IEEE Photon. Technol. Lett.*, vol. 10, pp. 397–399, Mar. 1998.
[30] R. Trebino, *Frequency-Resolved Optical Gating: The Measurement of Ultrafast Laser Pulses*. Boston, MA: Kluwer Academic, 2000.
[31] W. Kornelis, J. Biegert, J. W. G. Tisch, M. Nisoli, G. Sansone, C. Vozzi, S. De Silvestri, and U. Keller, "Single-shot kilohertz characterization of ultrafast pulses by spectral phase interferometry for direct electric-field reconstruction," *Opt. Lett.*, vol. 28, pp. 281–283, Feb. 2003.
[32] C. W. Siders, J. L. W. Siders, A. J. Taylor, S.-G. Park, and A. M. Weiner, "Efficient high energy pulse train generation using a 2^n-pulse Michelson interferometer," *Appl. Opt.*, vol. 37, pp. 5302–5305, Aug. 1998.
[33] G. Imeshev, M. A. Arbore, M. M. Fejer, A. Galvanauskas, M. Fermann, and D. Harter, "Ultrafast-pulse second-harmonic generation with longitudinally nonuniform quasiphase-matching gratings: pulse compression and shaping," *J. Opt. Soc. Amer. B*, vol. 17, pp. 304–318, Feb. 2000.
[34] A. M. Weiner, "Femtosecond optical pulse shaping and processing," *Prog. Quantum Electron.*, vol. 19, pp. 161–237, 1995.
[35] M. Rahm, U. Bader, G. Anstett, J.-P. Meyn, R. Wallenstein, and A. Borsutzky, "Pulse-to-pulse wavelength tuning of an injection seeded nanosecond optical parametric generator with 10 kHz repetition rate," *Appl. Phys. B Lasers O.*, vol. 75, pp. 47–51, July 2002.

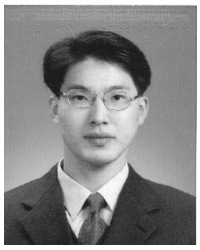

Jung-Ho Chung (S'01) received the B.S. degree in electrical engineering from Seoul National University, Seoul, Korea, in 1997 and the M.S. degree in electrical and computer engineering from Purdue University, West Lafayette, IN, in 2001, where he is currently pursuing the Ph.D. degree in electrical and computer engineering.

Until 1999, he worked on code-division multiple-access communication systems at KTF, Seoul. At Purdue University, he is doing research in the Ultrafast Optics and Optical Fiber Communications Laboratory on space–time processing of ultrafast optical pulses, as well as ultrafast pulse measurement techniques.

Mr. Chung received a Student Travel Award (2001) and a Graduate Student Fellowship (2003) from the IEEE Lasers & Electro-Optics Society (LEOS).

Andrew M. Weiner (S'84–M'84–SM'91–F'95) received the Sc.D. degree in electrical engineering from the Massachusetts Institute of Technology (MIT), Cambridge, in 1984.

From 1979 through 1984, he was a Fannie and John Hertz Foundation Graduate Fellow at MIT. In 1984, he joined Bellcore, where in 1989, he became manager of ultrafast optics and optical signal processing. He joined Purdue University, West Lafayette, IN, in 1992 as Professor of Electrical and Computer Engineering. He is currently the Scifres Distinguished Professor of Electrical and Computer Engineering (ECE) as well as ECE Director of Graduate Admissions. His research focuses on ultrafast optical signal processing and high-speed optical communications. He is especially well known for pioneering the field of femtosecond pulse shaping, which enables generation of nearly arbitrary ultrafast optical waveforms according to user specification. He has published four book chapters and more than 120 journal articles. He has been author or coauthor of more than 200 conference papers, including approximately 60 conference invited talks, and has presented more than 50 additional invited seminars at universities or industry. He has received five U.S. patents.

Prof. Weiner is a Fellow of the Optical Society of America (OSA). He has received numerous awards for his research, including the Hertz Foundation Doctoral Thesis Prize (1984), the Adolph Lomb Medal of the Optical Society of America (1990), awarded for pioneering contributions to the field of optics made before the age of 30, the Curtis McGraw Research Award of the American Society of Engineering Education (1997), the International Commission on Optics Prize (1997), the IEEE LEOS William Streifer Scientific Achievement Award (1999), the Alexander von Humboldt Foundation Research Award for Senior U.S. Scientists (2000), and the inaugural Research Excellence Award from the Schools of Engineering at Purdue. He has served on or chaired numerous research review panels, professional society award committees, and conference program committees. In 1988–1989, he served as an IEEE Lasers and Electro-Optics Society (LEOS) Distinguished Lecturer. He was General Co-Chair of the 1998 Conference on Lasers and Electro-Optics, Chair of the 1999 Gordon Conference on Nonlinear Optics and Lasers, and Program Cochair of the 2002 International Conference on Ultrafast Phenomena. In addition, he was Associate Editor for IEEE JOURNAL OF QUANTUM ELECTRONICS, IEEE PHOTONICS TECHNOLOGY LETTERS, and *Optics Letters*. Prof. Weiner was an elected member of the Board of Governors of IEEE LEOS from 1997 to 1999 and Secretary/Treasurer of IEEE LEOS from 2000 to 2002.